High-Speed Visualization of Spray Breakup and Velocity Estimation in a Rotating Detonation Combustor Using Laser Induced Fluorescence

Matthew W. Hoeper*
RTX Research Center, East Hartford, CT 06108, USA

Robert B. Wang [†], Peter E. Salek [‡], Zoe E. Brand [§], Venkat Athmananthan [¶] Terrence R. Meyer[‖]
School of Mechanical Engineering, Purdue University, W. Lafayette, IN 47907, USA

Austin M. Webb **, Christopher A. Fugger [††]
Spectral Energies LLC, 4065 Executive Dr, Beavercreek, OH 45430

H. Douglas Perkins [‡‡]
NASA Glenn Research Center, Cleveland, OH 43315, USA

The underlying physical processes that liquid fuel sprays undergo in rotating detonation engines, particularly breakup and combustion, are not well understood nor are the coupling effects between the detonation and the spray. In this work, a single liquid jet of liquid fuel is inserted into a hydrogen-air RDC in order to study repetitive-one way coupled detonation interactions. High speed laser induced fluorescence of Jet-A at 300 kHz is used to visualize the dynamic processes inside the RDC for up to 10 ms per test. The employed imaging schemes allowed for unique insight into the the spreading of liquid fuel in the azimuthal-axial directions via volumetric laser illumination. The Jet-A velocity field was estimated using OpenOpticalFlow and the impulse events observed colloquially agree with prior work on this test platform.

I. Nomenclature

BFS = backwards facing step
RDC = rotating detonation combustor
PLIF = planar laser induced fluorescence

II. Introduction

Detonation based propulsion and energy generation has received a tremendous amount of attention in the last several years due to the potential increase in thermodynamic efficiency over current generation combustion devices [1]. One of the more promising systems is the rotating detonation combustor (RDC). Typically, RDCs operate in a non-premixed fashion where the reactants are injected into an annular combustion chamber. A detonation wave travels azimuthally around the gap, consuming the mixed reactants. The product gases, trailing the detonation wave, attain pressures several times higher than the initial reactants. Detonation wave speeds range between 1-2 km/s, and are typically in the range of 60-80% of the Chapman-Jouguet (C-J) velocity around the annulus. Reactant refill must transpire within tens to

*Sr. Research Engineer (formerly Doctoral Student at Purdue University)
[†]Doctoral Student, School of Mechanical Engineering
[‡]Doctoral Student, School of Mechanical Engineering
[§]Graduate Student, School of Mechanical Engineering
[¶]Senior Research Scientist, School of Mechanical Engineering
[‖]Professor, School of Mechanical Engineering and School of Aerospace and Aeronautics (by Courtesy)
**Aerospace Engineer
[††]Aerospace Engineer
[‡‡]Aerospace Engineer

hundreds of microseconds to sustain pseudo-stable operation, supporting the formation of single or multiple waves. The highly unsteady and periodic nature of these devices present unique challenges for researchers both numerically and experimentally.

Much of the research on RDCs has been predominately focused on systems that operate with gaseous reactants. However, recently, multi-phase reactants including liquid-gas and liquid-liquid systems have gained traction in recent years for fundamental experiments as well as full combustor evaluation [2–18]. The use of liquid propellants introduces additional complexity beyond gas-gas systems due to additional physical processes such as spray breakup, droplet atomization, and spray combustion. These processes could further complicate the dynamic stability and operability of an RDC. Currently, the experimental research on fundamental spray properties and behavior in denotation environments and for relevant RDC geometries is sparse. Anderson et al. conducted experiments to emulate liquid injector response from a detonation wave by using a single detonation wave that exhausts into a chamber where the breakup of liquid jet would be measured with a high speed camera [14]. Hoeper et al. [2] and Black et al. [3] have performed time resolved PLIF imaging of liquid jets in an RDC and a linear detonation channel, respectively. Both of these works have showcased the dynamic nature of liquid jets subject to repetitive, impulsive loading from detonation waves. Measurements of droplet size distributions in RDC-like geometry was reported by Liu et al where simultaneous PLIF and Mie scattering images were used to infer the droplet size in a linearized detonation combustor [5]. This appears to be the only publication that reports experimental droplet size distributions in a detonation device. Sophisticated numerical simulations of two-phase RDEs are also underway [19–24]. Currently, state-of-the-art simulations lack experimental data to validate these results. Additionally, there is a need for fundamental research concerning the physical processes at the scale of individual injector elements. Therefore, it is critical to have experimental information on the fuel distributions within these devices and how they respond to detonation waves. Knowledge of the aforementioned processes will be imperative for tuning RDC operation as well as for model validation. This study seeks to extend that work and to provide a more comprehensive picture of how a single liquid spray of Jet-A responds and reacts to repetitive, impulsive loading from a detonation wave in relevant conditions.

III. Experimental Methods

A. Rotating Detonation Combustor

The RDC platform used in this work has been reported in several other works including characterization of a single liquid fuel injector [2, 25–27]. The RDC operates using hydrogen-air and is ignited by a H_2-O_2 pre-detonator. For this work, the RDC was modified to incorporate a single liquid fuel injector for one-way coupled detonation interaction studies. The combustion chamber has an inner diameter of 114.3 mm, a channel width of 10.7 mm, and a length of 90 mm. Ambient temperature air flows through an annular converging-diverging nozzle with a throat gap of 1.42 mm. The flow then expands at an angle of 10°. At an area ratio of 1.6, the expansion ends with a backwards facing step (BFS) which marks the entrance of the detonation channel. Hydrogen is injected radially through 99 orifices that reside on the air expansion geometry. The spacing between orifices is 3.6° except for one location where there is a gap of 7.2° as shown in the top left of Figure 1. This gap is coincides with the azimuthal location of the liquid fuel injector which sits in the BFS. The working liquid fuel was Jet-A in this work. The liquid fuel injector is 3D printed from stainless steel and has an internal cylindrical plenum with a diameter of 3 mm and a final exit diameter of 0.3 mm. The orifice injects fuel axially and is positioned at the mid-radius of the detonation channel as noted in Figure 1. An optically clear outerbody constructed from Dow Corning 7980 is used to provide optical access. The hardware configuration discussed herein is common across all experiments presented. During a test, the RDC is fired for around 500 ms which includes a $\sim$ 50 ms long startup period after which the combustor settles into a 1 wave operating mode near 4 kHz. LIF images are captured at around the 400 ms mark. For this work, two chamber conditions and two injector pressure drops were considered which are shown in Table 1. The equivalence ratio between the primary reactants, H2-air, is maintained at 1 for all tests. The nominal detonation wave speed is between 1450-1550 m/s for all conditions.

B. Optical System

The illumination and imaging scheme that was used in prior work by Hoeper et al. [28] is useful for measurement of liquid fuel distribution in the radial-axial plane. Wherein, a sub millimeter thick laser sheet illuminates a diesel spray during the refill process at up 1 MHz. However, the primary drawback with this method is the absence of azimuthal spray information. Any transport of liquid fuel in the azimuthal direction is unable to be captured. For the work presented in

Table 1 Test conditions for hot fire experiments. Table values represent the mean across multiple tests.

Test Condition	Air Mass Flow Rate [kg/s]	Liquid Inj. Pressure [bar]	Chamber Mass Flux [kg/m^2/s]
1	0.23	2.7	57
2	0.23	2.7	57
3	0.46	8.9	110
4	0.46	8.9	110

this study, the orientation of the camera and laser enable imaging the azimuthal-axial plane through volumetric or "slab" illumination. This enables measurements of the liquid fuel responding and spreading due to the impulsive loading from the detonation wave. A schematic of this is shown in Figure 1. Due to the tangential positioning of the primary imaging plane to the RDC geometry the LIF images must be dewarped and re-projected onto a rectilinear plane. This process was performed with LaVision's DaVis 10 software [29]. The field of view of the LIF images is quite small and has minimal distortion. Most of the corrections are for barrel distortion near the edges of the image.

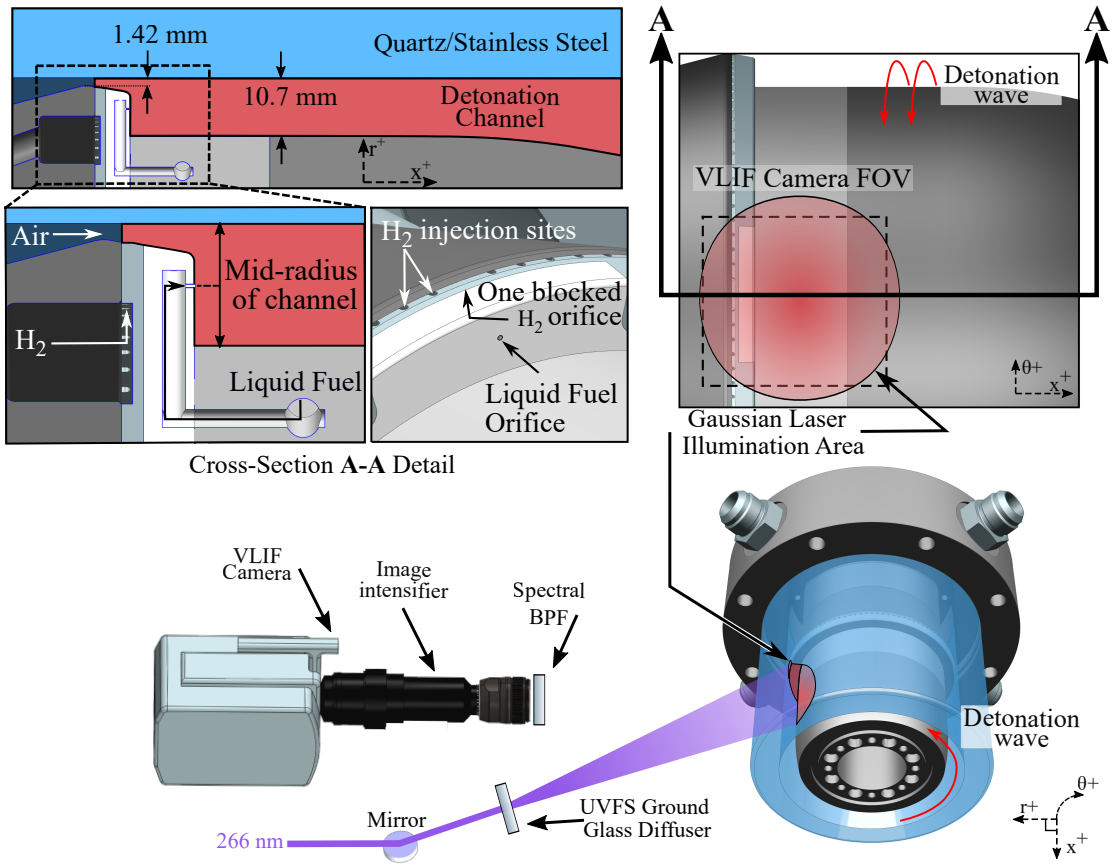

Fig. 1 Schematic depicting key combustor geometries and optical arrangement.

A burst mode laser operating at 300 kHz was tuned to output 5 ns pulses at a wavelength of 266 nm for excitation of Jet-A. A 120 grit UVFS ground glass diffuser (THORLABS: DGUV10-120) was placed around 250 mm from the combustor to act as a beam expander. The diffuser creates a near ideal Gaussian distribution that is projected over the liquid fuel injection area. The beam was expanded to be slightly larger than the imaging area and so no additional expansion lenses were used. The spot size is large enough so that the tails of the Gaussian distribution are not being

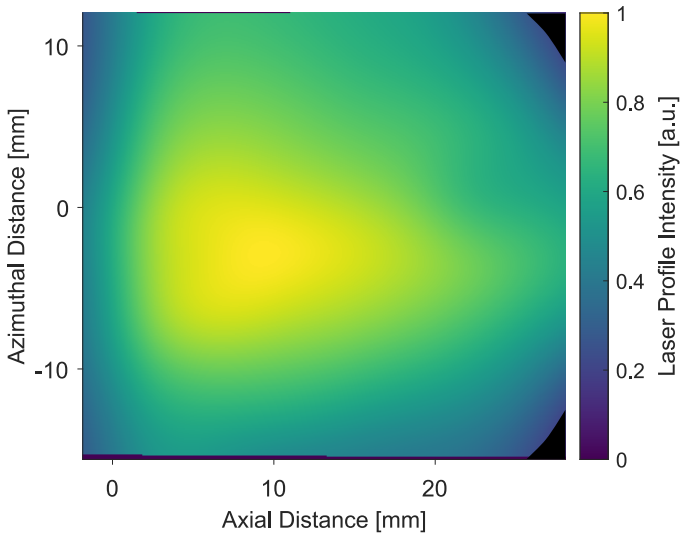

Fig. 2 Typical laser intensity profile as imaged by the high speed camera.

used inside the camera field of view. An example of the laser intensity profile is shown in Figure 2 where the 0,0 point is the liquid fuel injector exit plane. Approximately 300 µJ per pulse was used in 10 ms bursts which is equal to around 35 detonation periods. The Jet-A emission was imaged with a Phantom TMX 7510 that was paired with a UV-Visible HiCATT image intensifier operating at the same frequency as the laser. A 105 mm UV $f/4.5$ lens was used with a 40 ns gate to eliminate background flame luminosity. The camera was used in binned mode which allows the full physical dimensions of the camera chip to be used at 300 kHz but at half the spatial resolution. In binned mode, the spatial resolution was 14 px/mm with an overall interrogation region of 25 mm × 30 mm. A 315-475 nm bandpass filter was used to isolate the emission wavelengths while also suppressing scattering of the laser and additional background light.

Filtered chemiluminescence imaging was also performed in separate experiments to support the LIF results. The test conditions of the LIF experiments were repeated for OH* and CH* imaging. Similarly, a TMX 7510 paired with a UV-Visible HiCATT image intensifier operating at 250 kHz was used for this purpose. The orientation of the camera was identical to what is shown in Figure 1 but with a larger field of view. The CH* tests used a 105 mm $f/4$ visible lens with two spectral filters: a 433±12 and a 450±25 nm band pass filter. The OH* configuration used a 105 $f/5.6$ UV lens and a 320±20 nm bandpass filter. The average spatial resolution was 8.4 pixel/mm and a 200 ns gate was used in all cases. A smaller aperture was used to remediate focal depth effects.

IV. Results and Discussion

To introduce the LIF results, a time-series of LIF images are shown in Figure 3 that span a full detonation period. The test corresponds to condition 2. The Figure shows every 5th frame of the original data (16.67 µs) for brevity and have the same contrast scaling. The frames are denoted by the approximate phase angle which was computed by equating the number of frames between wave passes to be 360°. A phase angle of $\theta = 0°$ was assigned ot the point in time at which the maximum rate of change of signal intensity occurred. The method is fairly repeatable but could have an associated error of ±5°. The dark region near the jet core represents a dead-zone in the phosphor plate of the image intensifier.

The detonation wave passes through the center line of the spray in the $\theta = 4°$ frame and is traveling from bottom to top. The loss in apparent LIF signal is attributed to an optical effect because the signal recovers immediately. There is a significant pressure and temperature rise in the surrounding environment when the detonation wave passes over the jet core. This abrupt change will undoubtedly affect quenching rates of the excited Jet-A molecules. There is a general consensus that LIF signal is proportional to the volume of a liquid droplet. However, in this case, the overall fluence level is quite low and it is probable that the penetration of laser energy into the extremely dense core is shallow. Therefore, it is assumed most of the LIF signal is primarily originating from the surface of the jet core and is influenced by the enhanced quenching immediately behind the detonation wave. Furthermore, the emission spectra of Jet-A is around 40 nm FWHM around 310-350 nm from a 266 nm excitation source and there is also a weaker emission band

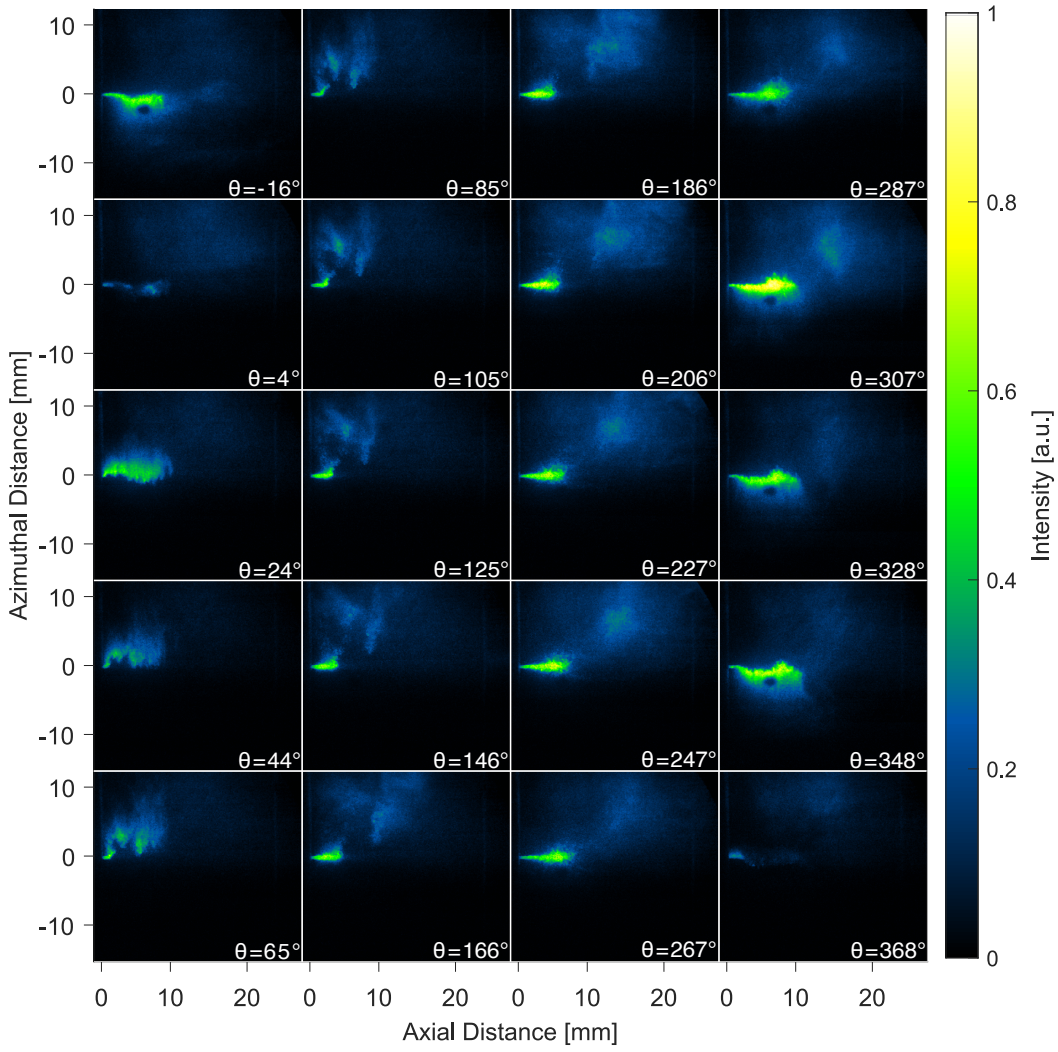

Fig. 3 A time sequence of LIF images showcasing a full cycle. Frames are labeled with an approximate phase angle. At $-16°$, the detonation is just out of frame and passes through the spray just prior to $4°$ and again near $368°$. The detonation wave is propagating from bottom to top.

between 290-310 nm [30]. Therefore, it is unlikely that the dense region trailing the detonation wave is absorbing the LIF emission in an appreciable way. A brief search of absorption lines in this range and around the excitation wavelength was performed on key combustion radicals through LIFBase and SpectraPlot [31, 32]. A possible candidate is the OH absorption band near 309 nm but even at elevated pressure the lines are only a few wavenumbers wide (less than 0.1 nm) much less than the bandwidth of the Jet-A emission. OH has an absorption line at 266.702 nm but even with pressure broadening the narrow line-width of the excitation laser at 266.075 nm ensures minimal spectral overlap. Jet-A vapor fluorescence has been reported to be fairly insensitive to pressure increase in a nitrogen atmosphere but is significantly reduced by increased temperature and oxygen presence which could explain the loss in signal [30].

Broadly speaking all the test conditions have similar spray behavior and the differences will be discussed. The following is a high-level description of key events during the detonation cycle. There are two distinct regions to the spray in the first two frames of Figure 3. A dense area around the core of the spray and a much more diffuse area surrounding the negative azimuthal side. Immediately following the passing of the detonation wave the spray is displaced and spreads into the direction of travel in the $\theta = 24°$ frame. Over the course of next 5 frames the fuel spray continues to become increasingly diffuse. Meanwhile the injector has already recovered and is issuing new fuel into the combustor. The fuel spray continues to recover unperturbed until around $\theta = 287°$. At this point, a sudden weak disturbance traveling in the

opposite azimuthal direction disturbs the spray. This causes the spray to displace and further spread which is evident by comparing the upper edge of the spray in the $\theta = 287°$ frame to the $\theta = 348°$ frame. The profile deflects into a highly irregular profile from a nearly straight line. The detonation wave passes through the spray center-line once again in the final frame. The process outlined above is common to all conditions in Table 1 and specific details will be subsequently discussed.

To show off the differences in spray distribution between the four test conditions, a comparison is shown in Figure 4. Each quadrant shows two overlaid instantaneous images from the same hot fire test each with a different color scheme. The green signal represents the maximum extent of the spray ~ 3 µs before the counter diffusion process begins. The magenta images are taken ~ 3µs prior to the detonation wave entering the frame. The bottom row's images are mirrored about the injection azimuth for clarity. The higher chamber mass flow rate condition is on the top row and higher liquid fuel injection pressures are on the left column. Overall, the behavior and spreading of the fuel is similar across each quadrant. In the case of higher air mass flow rates, there appears to be enhanced entrainment of liquid fuel into the air stream. It is believed the wake of the underexpanded jet emanating from the air as it enters the detonation channel is interacting with the top of the fuel spray where droplets are being stripped off and advected downstream. This is denoted as Region 1 in Figure 4. The regions marked by the dashed lines represent the region of Jet-A that was previously in the jet core and was broken up by the detonation wave. Figure 4(d) also has this region marked but it exists much closer to the BFS. In this case, the fuel dwells for much longer because the fuel jet does not penetrate very far into the channel and is sheltered from the air stream recovery for a longer time. Frame (c) does not experience this because the penetration is far enough into the channel. Region 2 shows wetting of the BFS with Jet-A immediately following the detonation wave. For much of the cycle time, after the detonation wave, the wetting of the wall is slowly stripped away.

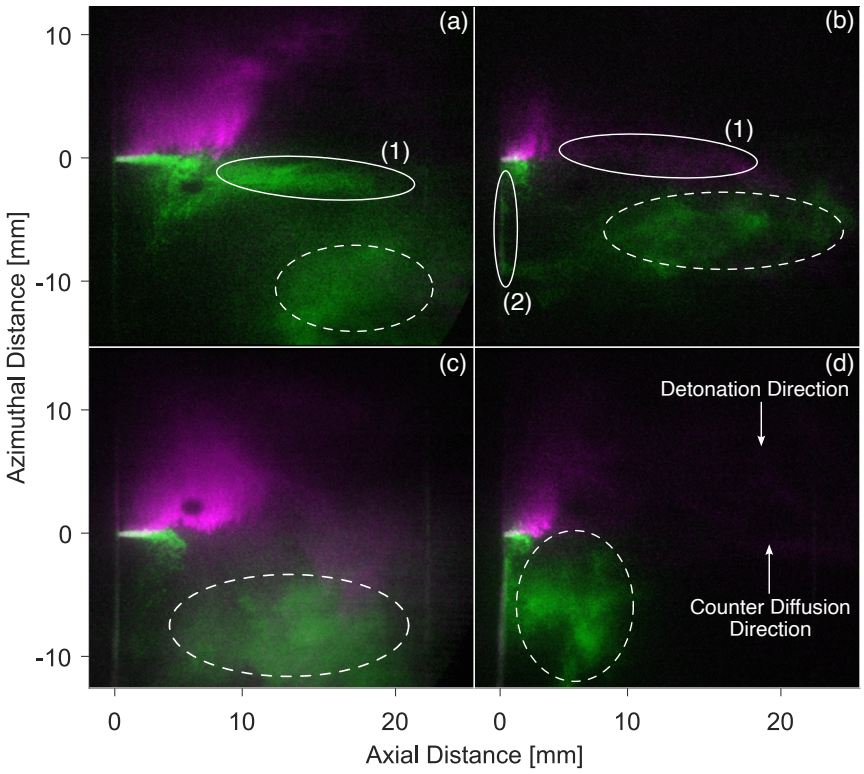

Fig. 4 Each quadrant shows two frames from a test. Green is the maximum extend of the spray before the counter diffusion mode begins. Magenta is the maximum extent of the spray just before the detonation wave arrives. (a), (b) and (c),(d) represent 0.45 kg/s and 0.23 kg/s, respectively. Left column has high liquid injection pressure.

V. Velocity Estimation Through Optical Flow

Optical flow is a technique commonly used in computer vision applications to extract displacements from brightness patterns in a pair of images. In engineering applications, optical flow has been applied to extract velocity fields from images taken from particle laden flows, combusting flows, and more. For this work, the freely available, open source software package OpenOpticalFlow is used to velocity estimation [33]. Liu and Shen developed a physics-based approach to solving optical flow problems and details can be found therein [34]. The authors developed a for researchers to use. Preliminary velocity estimations were calculated with LaVision's Davis 10 PIV software but it could not reliably track the diffuse regions of the LIF images. Specific details regarding the image processing procedure can be found in the OpenOpticalFlow paper but some high level details will be outlined here.

A pair of images are chosen for evaluation and the pair of images have a global intensity correction applied. The burst mode laser has decreasing pulse energies in later time but typically the variation between two sequential images is minimal so the corrections are small. Moreover, a similar assumption is made with the change in the Jet-A presence. Typically for optical velocity estimation, a passive scalar is required. Yet, it is apparent the Jet-A is undergoing evaporation and burning. However, considering the imaging rate it is assumed that the change between a pair of images is small enough such that optical flow can applied. For a pair of images the following procedure is taken. A smoothing Gaussian filter is applied to both images to remove noise. Both images are then down-sampled to half of their original size for an initial velocity field estimation. For example, a 500×500 pixel image will be spatially averaged to become a 250×250 pixel image that encompass the same spatial area. The initial velocity field is estimated by the Horn-Schunck method [35]. Subsequent velocity calculations iterate on the initial estimate up-sampled to the original image resolution through a Lagrange multiplier approach described by Liu [33].

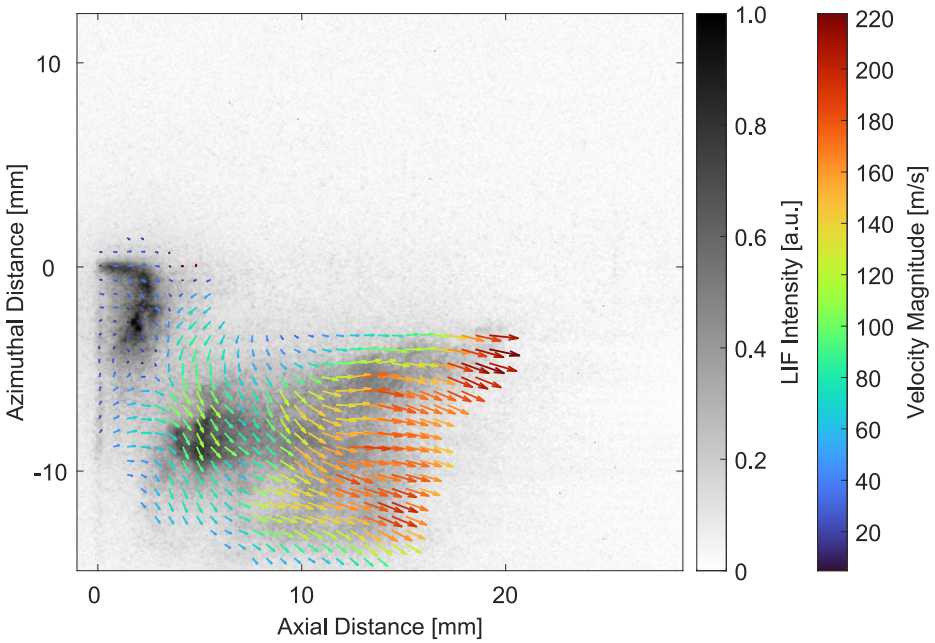

Fig. 5 An instantaneous LIF image overlaid with computed velocity vectors colored by magnitude

Optical flow estimates the velocity field at every pixel in the image and will attempt to determine the velocity field even in areas where only background noise is present. Care must be taken when post processing the resulting velocity fields to ensure regions with no signal are not included in any statistics. The following post processing approach is performed. First, a rolling Gaussian smoothing filter is applied to the LIF image with a 10 pixel standard deviation. The smoothed image is then binarized to determine which areas of the image have Jet-A present. The binarized image undergoes dilation to increase the size of the region by 3 pixels in all directions to provide a small tolerance to areas with strong gradients near the edge of the image. The dilated binarized image is then used as a mask against the computed velocity fields so that areas with very weak or no LIF signal are ignored. An example result of this procedure is shown in Figure 5 where the computed velocity field is overlaid atop a LIF image. The LIF image corresponds to condition 4 approximately 60 µs after the detonation wave pass. The spray has had some time to recover at this point and much of

the Jet-A that was broken up from the detonation wave is being entrained in the air stream with velocities up to 220 m/s. The velocity in the vicinity of the injector is 30-40 m/s which is the near the expected velocity from continuity. It is important to note that the post-processing procedure has drawbacks and some regions of noise will occasionally be counted and so there may be a slight overprediction of velocities at or near 0 m/s.

It is of interest to evaluate the velocity field for an entire cycle. Due to the number of LIF images per test, the velocity field can be condensed down to a phase averaged result. To achieve this, the pixel intensity near the injector is sampled as a function time. The resulting profile is smoothed by a rolling Gaussian filter. The gradient of the smoothed curve is calculated and the point with the greatest negative slope is assigned a phase angle of 0 degrees. The frames between two 0° are assigned a constant slope from 0° to 360°. LIF images are grouped with other images with similar phase angles. The indices within a phase angle group are used to identify the matching velocity field results. Around 25 velocity fields are averaged for each group. As mentioned earlier, optical flow can suffer from low SNR and so the last 1 ms of the laser burst is not included in the optical flow calculations. The process is performed for both axial and azimuthal velocities. From there each phase angle velocity result is converted into a probability distribution function.

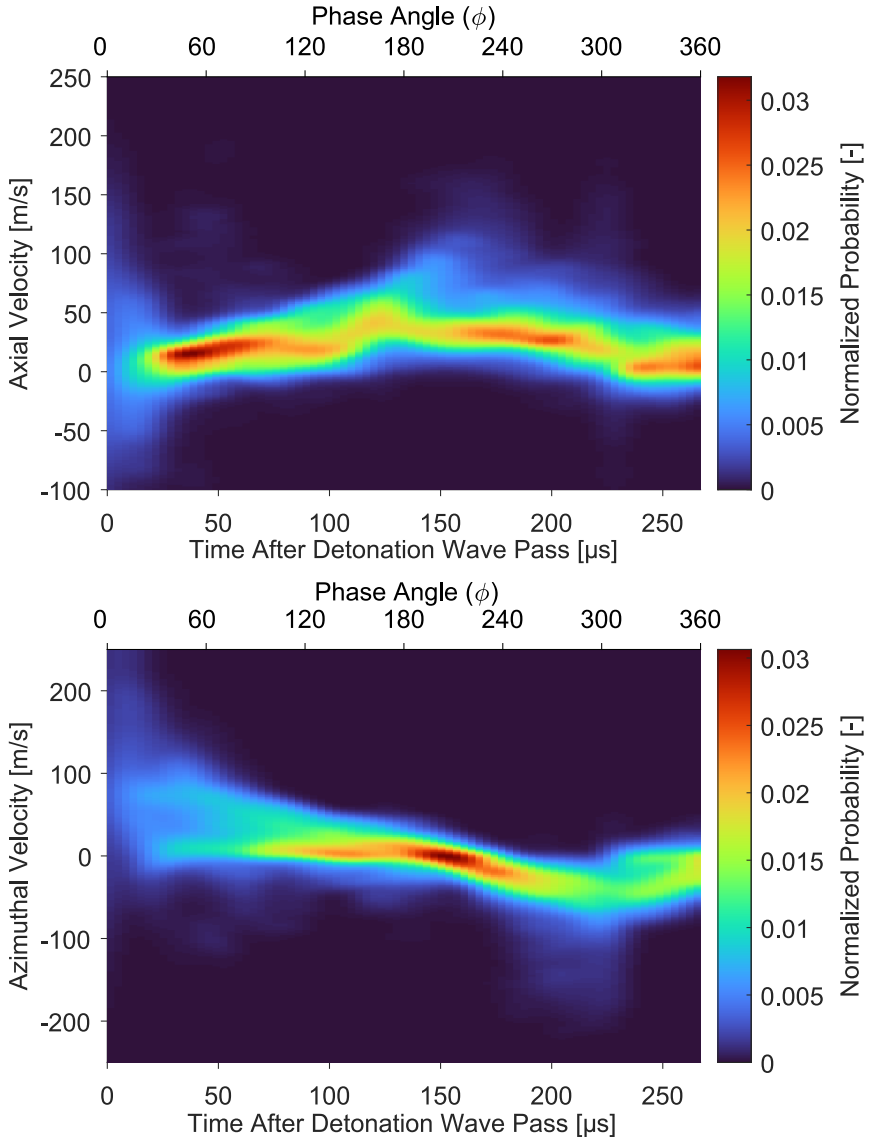

Fig. 6 Typical laser intensity profile as imaged by the high speed camera.

Figures 6 and 7 represent this final result. Each column in the image represent a computed PDF for both axial and

azimuthal velocity. The direction of positive azimuthal velocity is defined to be the direction of the wave. In Figure 6, it is evident that shortly after the denotation wave pass most of the axial velocity component is concentrated around -5 to 25 m/s. As time goes on the edge of the distribution on the positive side increases steadily until around 120 µs. At this point, based on the results from Hoeper et al. [2], the air stream is beginning the recovery process. Which for this chamber mass flux occurs around 40% of the way through the detonation cycle. Once this begins there is a steep acceleration observed in the axial velocity until around 180 µs where a noticeable drop in velocity occurs. This is not a deceleration of the Jet-A but rather parcels of Jet-A that underwent acceleration early on now exiting the field of view. This would correspond to Jet-A that previously made up the jet core just prior to the detonation wave passing. Once the high speed parcel of Jet-A has left the field of view much of the velocity content is composed of the fluid near the core and is relatively sheltered from the air-stream because of the BFS. The azimuthal velocity distribution in Figure 6 also shows an interesting trend. Immediately following the detonation there is significant positive velocity because much of the spray was impacted by the detonation wave. Following, the azimuthal velocity trends towards zero and maintains a very small negative velocity component which originates from Jet-A that is right next to the BFS. At around 160 µs there is a sharp change in the distribution which is from the counter diffusion mode.

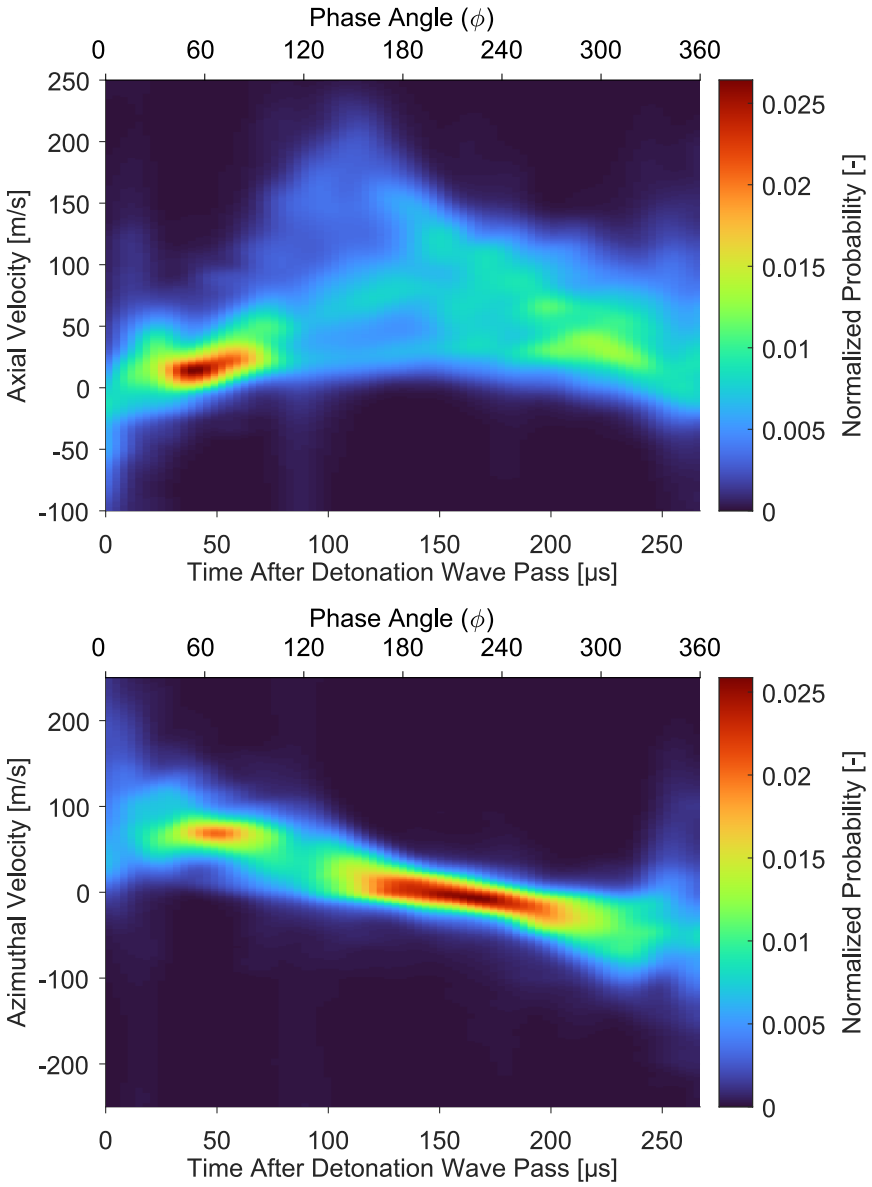

Fig. 7 Typical laser intensity profile as imaged by the high speed camera.

Figure 7 show very similar results but has an accelerated time scale. Within 50 µs there is steep acceleration of the Jet-A in the axial direction. Once again this matches well with the 20% cycle recovery time for this chamber mass flux per Hoeper et al. [2]. The decrease in velocity after 120 µs is a result of the same phenomena as discussed; the leading parcel of Jet-A accelerates and exits the field view which decreases the overall velocity distribution. The axial velocity distribution steadies out between 180-250 µs which appears to agree with Hoeper et al. [2] in that the higher air mass flow rate recovers to a quasi steady state for a short time before the detonation wave arrives. For this condition, the counter diffusion process does not appear as strongly nor as impulsive but it is present, nonetheless.

VI. Conclusion

The dynamics of a single element liquid Jet-A spray subject to repetitive detonation loading was studied with high speed laser induced fluorescence at 300 kHz in a hydrogen-air RDC. The azimuthal spreading of the fuel spray due to the detonation wave was captured through a volumetric laser illumination scheme. Additionally, minor physical process were identified across multiple chamber conditions. One such phenomena is a counter propagating event that displaces the recovered fuel spray very late into the cycle. This event further atomizes the spray ahead of the detonation. The velocity field of the Jet-A spray was estimated throughout the the entire cycle through the use of optical flow. Near field velocities were observed as high as 150 and 250 m/s in the axial direction for air mass flow rates of 0.23 and 0.46 kg/s, respectively. These velocities are not sustained, however. Parcels of Jet-A that make up the jet core are displaced significantly due to the detonation wave. The spray is likely spreading in all directions including radially which promotes entrainment in the air stream as the air recovers. The time into the detonation where axial velocities undergo rapid acceleration agrees well with prior work into the refill statistics of this test platform.

Appendix

While not the focus of this work it may be useful to briefly discuss the nature of the counter propagating mode observed in the LIF images. For the chamber condition represented in Figure 3 (0.23 kg/s) the counter propagating mode occurs every detonation cycle and is a short lived event. However, in the case of the higher air mass flow rate the event typically occurs on an every-other cycle basis. Figure 8 shows a time series of LIF images for two full detonation periods. Between frames 8 and 9 there is a detonation wave pass but there is no spreading from the counter propagating mode as seen in the first and final frames. The counter diffusion process does not appear to be a single impulse event in this result based on the deflection of the jet core lasting up to 100 µs in some cases.

Filtered CH* and OH* imaging was used to determine the level of reactivity of this counter propagating event. The chemiluminescence was not collected simultaneously with the LIF so to facilitate a means of comparison, only phase averaged chemiluminescence images are considered. For each test a total of 5000 images at 250 kHz were recorded which is around 80 detonation periods. The processing pathway is outline below. First, a binarization mask is applied and the average binary value is calculated across the axial direction. This results in a $1 \times N$ profile where N is the number of pixels in the azimuthal direction of the dewarped image. The resulting intensity profile is then smoothed with a Butterworth filter to make gradient computations and searching easier. The value and location of the maximum signal along the profile is found. Based on the wave direction, only the leading side is considered for this step. If the maximum value of the profile does not exceed 1.5 times the mean value, the image is assumed to have no wave front and is not included in future computations. A search window of +/- 50 pixels from the peak signal location is evaluated for the location of the maximum derivative. This location is treated as the detonation wave front and based on the azimuthal location of the wave front, a phase angle is assigned to the original image. This procedure is applied to all images from the test. Images are then grouped into $\pm 2^\circ$ bins based on the computed phase angle and averaged. In the case where the detonation front is no longer a strong gradient or has passed beyond the field of view an average phase angle velocity is used to approximate the phase angle of subsequent frames. For example, beyond a phase angle of $+5^\circ$ the detonation front becomes too diffuse in the CH* images for a proper wave front location to be determined using the method outline above. To construct the phase averaged result, the rate of change of the phase angle in the image set is determined between $\theta = -30 \circ to 5 \circ$. That rate is assumed to be constant and is assigned to following frames. So if the phase angle velocity was 4.5 °/s, the first frame beyond the 5° mark would have a phase angle of 9.5 °, the second, 14° and so on. The OH* images undergo the same procedure but is only necessary after +30° once the detonation wave passes beyond the camera field of view.

Figure 9 shows an example of the phase averaging result for the CH* images. In the first frame ($\theta = -28$) there is a faint region of signal below the -25 mm azimuth as the detonation wave enters the field of view. The signal then

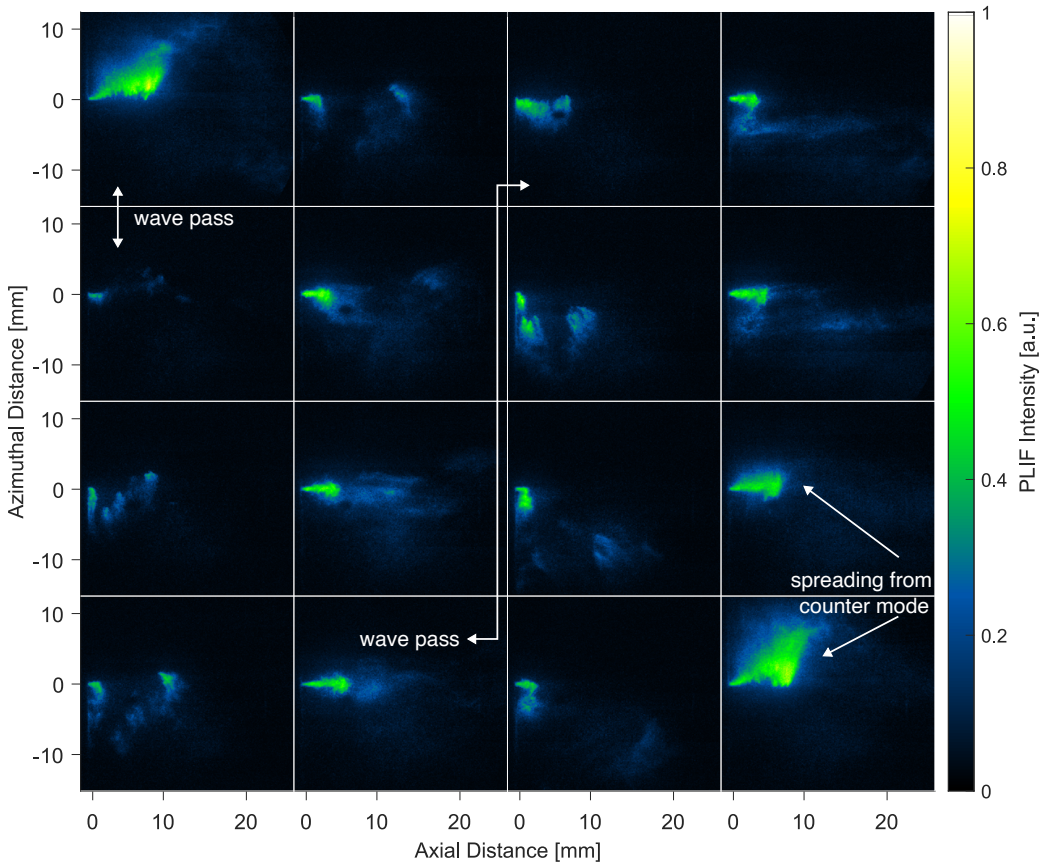

Fig. 8 Time series of LIF images showing two denotation periods for the higher mass flux case.

increases sharply as the number density of Jet-A increases from the wave reference frame. This continues until around $\theta = 4$ where the CH* flow field begins to separate into two zones marked by white circles. Region 1 is where the dense jet core resides hence why the reaction area is dragged so far in the azimuthal direction. Conversely, region 2 represents an area where Jet-A exists but in a more diffuse manner which promotes the shorter reaction zone. Residual burning is present long after the wave pass and the CH* does show some velocity gradient that is opposite the primary wave direction. Region 3 shows advection of a parcel of CH* traveling primarily in the axial direction but does have a slight azimuthal component. However, the timing of this event does not correspond with the counter propagation mode seen in the LIF images. Nothing appears in either the CH* or OH* images near a phase angle of 287° that would suggest the event is a reaction front. From this it is likely the counter propagating event is the result of an adverse pressure gradient that is driving the velocity in the opposite direction.

Acknowledgments

Matthew Hoeper would like to thank the support of the NASA Space Technologies Graduate Research Fellowship (NSTGRO) through Dr. H. Doug Perkins; grant number 80NSSC21K1293.

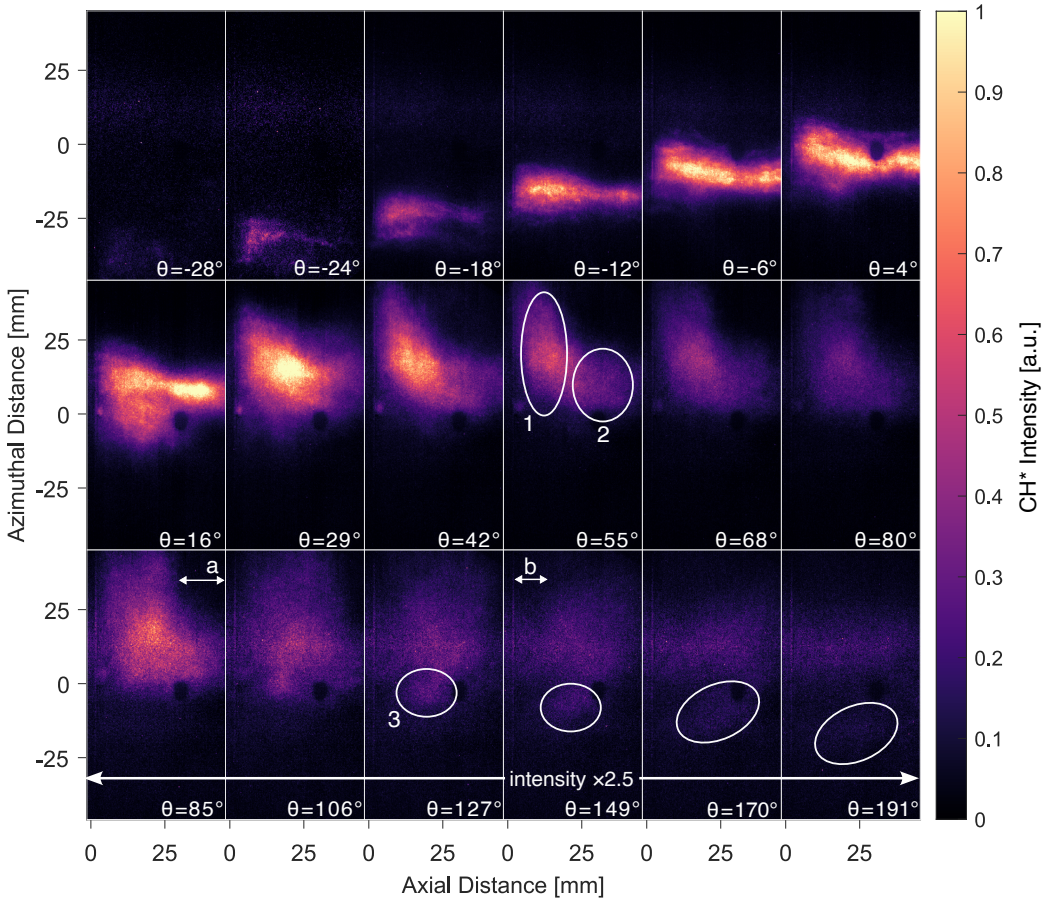

Fig. 9 A set of CH* phase averaged images for condition 2. Note the bottom row of images have the intensity scaled by a factor of 2.5

References

[1] Nordeen, C. A., Schwer, D., Schauer, F., Hoke, J., Barber, T., and Cetegen, B., "Thermodynamic model of a rotating detonation engine," *Combust., Explos., Shock Waves*, Vol. 50, No. 5, 2014, pp. 568–577.

[2] Hoeper, M. W., Webb, A. M., Athmanathan, V., Wang, R. B., Douglas Perkins, H., Roy, S., Meyer, T. R., and Fugger, C. A., "Liquid fuel refill dynamics in a rotating detonation combustor using megahertz planar laser-induced fluorescence," *Proceedings of the Combustion Institute*, 2022. https://doi.org/https://doi.org/10.1016/j.proci.2022.07.230.

[3] Black, C. H., Winter, T. R., Jackson, D. R., Frederick, M., Gejji, R., Slabaugh, C. D., Perkins, H. D., and Fugger, C. A., "Liquid Jet Response to Detonation Waves in a Linear Detonation Combustor," *AIAA SCITECH 2023 Forum*, 2023. https://doi.org/10.2514/6.2023-0356.

[4] Anderson, W. S., and Heister, S. D., "Response of a Liquid Jet in a Multiple Detonation Driven Crossflow," *2018 AIAA Aerospace Sciences Meeting*, 2018. https://doi.org/10.2514/6.2018-0635.

[5] Liu, H., Song, F., Jin, D., Yang, Z., Xu, S., and Yang, X., "Experimental Investigation of Kerosene Droplet Distribution in a Linearized Rotating Detonation Engine," *Combustion Science and Technology*, Vol. 0, No. 0, 2022, pp. 1–16. https://doi.org/10.1080/00102202.2022.2113393.

[6] Kubicki, S. W., Anderson, W., and Heister, S. D., "Further Experimental Study of a Hypergolically-Ignited Liquid-Liquid Rotating Detonation Rocket Engine," *AIAA Scitech 2020 Forum*, 2020. https://doi.org/10.2514/6.2020-0196.

[7] Nair, A. P., Keller, A. R., Minesi, N. Q., Pineda, D. I., and Spearrin, R. M., "Detonation cell size of liquid hypergolic propellants: Estimation from a non-premixed combustor," *Proceedings of the Combustion Institute*, 2022. https://doi.org/https://doi.org/10.1016/j.proci.2022.06.015.

[8] Teasley, T., Fedotowsky, T., Gradl, P., Austin, B., and Heister, S., "Current State of NASA Continuously Rotating Detonation Cycle Engine Development," *AIAA SCITECh 2023 Forum*, 2023. https://doi.org/https://doi.org/10.2514/6.2023-1873.

[9] Lim, D., "EXPERIMENTAL STUDIES OF LIQUID INJECTOR RESPONSE AND WALL HEAT FLUX IN A ROTATING DETONATION ROCKET ENGINE," Ph.D. thesis, Purdue University, 2019. https://doi.org/https://doi.org/10.25394/PGS.11113250.v1.

[10] Bykovskii, F. A., Zhdan, S. A., and Vedernikov, E. F., "Continuous spin detonation of fuel-air mixtures," *Combustion, Explosion and Shock Waves*, Vol. 42, 2006, pp. 463–471. https://doi.org/10.1007/s10573-006-0076-9.

[11] Wolański, P., Balicki, W., Perkowski, W., and Bilar, A., "Experimental research of liquid-fueled continuously rotating detonation chamber," *Shock Waves*, 2021, pp. 1–6. https://doi.org/10.1007/s00193-021-01014-w.

[12] Frolov, S. M., Shamshin, I. O., Aksenov, V. S., Gusev, P. A., Zelensky, V. A., Evstratov, E. V., and Alymov, M. I., "Rocket Engine with Continuously Rotating Liquid-Film Detonation," *Combustion Science and Technology*, 2020. https://doi.org/10.1080/00102202.2018.1557643.

[13] Dille, K. J., "TRANSIENT RESPONSE OF GAS-LIQUID INJECTORS SUBJECTED TO TRANSVERSE DETONATION WAVES," Master's thesis, Purdue University, 2020. https://doi.org/https://doi.org/10.25394/PGS.13075955.v1.

[14] Anderson, W. S., Lim, D., Washington, M. R., and Heister, S. D., "Experimental study of liquid injector elements for use in rotating detonation engines," 2017. https://doi.org/10.2514/6.2017-1932.

[15] Anderson, W. S., and Heister, S. D., "Response of a Liquid Jet in a Multiple Detonation Driven Crossflow," American Institute of Aeronautics and Astronautics, 2018. https://doi.org/10.2514/6.2018-0635, URL https://arc.aiaa.org/doi/10.2514/6.2018-0635.

[16] Malik, V., Salauddin, S., Hytovick, R., Bielawski, R., Raman, V., Bennewitz, J., Burr, J., Paulson, E., Hargus, W., and Ahmed, K., "Detonation wave driven by aerosolized liquid RP-2 spray," *Proceedings of the Combustion Institute*, Vol. 39, 2023, pp. 2807–2815. https://doi.org/10.1016/j.proci.2022.08.127.

[17] Jarsalé, G., Virot, F., and Chinnayya, A., "Ethylene–air detonation in water spray," *Shock Waves*, Vol. 26, 2016, pp. 561–572. https://doi.org/10.1007/s00193-016-0679-3.

[18] Benmahammed, M. A., Veyssiere, B., Khasainov, B. A., and Mar, M., "Effect of gaseous oxidizer composition on the detonability of isooctane-air sprays," *Combustion and Flame*, Vol. 165, 2016, pp. 198–207. https://doi.org/10.1016/j.combustflame.2015.12.004.

[19] Salvadori, M., Panchal, A., and Menon, S., "Simulation of liquid droplets combustion in a rotating detonation engine," *Proceedings of the Combustion Institute*, 2022. https://doi.org/https://doi.org/10.1016/j.proci.2022.09.002.

[20] Prakash, S., Bielawski, R., Raman, V., Ahmed, K., and Bennewitz, J., "Three-dimensional Numerical Simulations of a Liquid RP-2/O2 based Rotating Detonation Engine," *Combustion and Flame*, Vol. 259, 2024, p. 113097. https://doi.org/https://doi.org/10.1016/j.combustflame.2023.113097.

[21] Hayashi, A. K., Tsuboi, N., and Dzieminska, E., "Numerical study on JP-10/air detonation and rotating detonation engine," *AIAA journal*, Vol. 58, No. 12, 2020, pp. 5078–5094.

[22] Schwer, D. A., "Multi-dimensional simulations of liquid-fueled JP10/oxygen detonations," *AIAA Propulsion and Energy 2019 Forum*, 2019, p. 4042.

[23] Meng, Q., Zhao, N., and Zhang, H., "On the distributions of fuel droplets and in situ vapor in rotating detonation combustion with prevaporized n-heptane sprays," *Physics of Fluids*, Vol. 33, No. 4, 2021.

[24] Meng, Q., Zhao, M., Zheng, H., and Zhang, H., "Eulerian-Lagrangian modelling of rotating detonative combustion in partially pre-vaporized n-heptane sprays with hydrogen addition," *Fuel*, Vol. 290, 2021, p. 119808.

[25] Athmanathan, V., Braun, J., Ayers, Z. M., Fugger, C. A., Webb, A. M., Slipchenko, M. N., Paniagua, G., Roy, S., and Meyer, T. R., "On the effects of reactant stratification and wall curvature in non-premixed rotating detonation combustors," *Combustion and Flame*, Vol. 240, 2022, p. 112013. https://doi.org/10.1016/j.combustflame.2022.112013.

[26] Athmanathan, V., Rahman, K. A., Lauriola, D. K., Braun, J., Paniagua, G., Slipchenko, M. N., Roy, S., and Meyer, T. R., "Femtosecond/picosecond rotational coherent anti-Stokes Raman scattering thermometry in the exhaust of a rotating detonation combustor," *Combustion and Flame*, Vol. 231, 2021, pp. 111504–NA. https://doi.org/10.1016/j.combustflame.2021.111504.

[27] Hsu, P. S., Slipchenko, M. N., Jiang, N., Fugger, C. A., Webb, A. M., Athmanathan, V., Meyer, T. R., Roy, S., and Chrisesh, P. S. S. J. N. F., "Megahertz-rate OH planar laser-induced fluorescence imaging in a rotating detonation combustor." *Optics letters*, Vol. 45, 2020, pp. 5776–5779. https://doi.org/10.1364/ol.403199.

[28] Hoeper, M. W., Webb, A. M., Athmanathan, V., Wang, R. B., Douglas Perkins, H., Roy, S., Meyer, T. R., and Fugger, C. A., "Liquid fuel refill dynamics in a rotating detonation combustor using megahertz planar laser-induced fluorescence," *Proceedings of the Combustion Institute*, Vol. 39, No. 3, 2023, pp. 3051–3061. https://doi.org/https://doi.org/10.1016/j.proci.2022.07.230.

[29] LaVsion GmbH, "DaVis 10.2.0," , 2024. URL https://www.lavision.de/en/.

[30] Orai, M., Baranger, P., Ledier, C., Apeloig, J., and Grisch, F., "Fluorescence spectroscopy of kerosene vapour at high temperatures and pressures: potential for gas turbines measurements," *Applied Physics B*, 2014, pp. 729–745. https://doi.org/10.1007/s00340-013-5756-z.

[31] Luque, J., and Crosley, D., "LIFBASE: Database and Spectral Simulation Program," , 2021. URL https://www.sri.com/platform/lifbase-spectroscopy-tool/.

[32] Goldenstein, C. S., Miller, V. A., Mitchell Spearrin, R., and Strand, C. L., "SpectraPlot.com: Integrated spectroscopic modeling of atomic and molecular gases," *Journal of Quantitative Spectroscopy and Radiative Transfer*, Vol. 200, 2017, pp. 249–257. https://doi.org/https://doi.org/10.1016/j.jqsrt.2017.06.007.

[33] Liu, T., "OpenOpticalFlow: An Open Source Program for Extraction of Velocity Fields from Flow Visualization Images," *Jounral of Open Researh Software*, Vol. 5, 2017. https://doi.org/DOI:10.5334/jors.168.

[34] Liu, T., and SHEN, L., "Fluid flow and optical flow," *Journal of Fluid Mechanics*, Vol. 614, 2008, p. 253–291. https://doi.org/10.1017/S0022112008003273.

[35] Horn, B. K., and Schunck, B. G., "Determining optical flow," *Artificial Intelligence*, Vol. 17, No. 1, 1981, pp. 185–203. https://doi.org/https://doi.org/10.1016/0004-3702(81)90024-2.